nanomaterials

MDPI

Article

Synthesis of $Fe_{1-x}S$ Nanoparticles with Various Superstructures by a Simple Thermal Decomposition Route and Their Magnetic Properties

Aleksandr A. Spivakov, Chun-Rong Lin *, Yu-Chuan Chang and Ying-Zhen Chen

Department of Applied Physics, National Pingtung University, Pingtung County 90003, Taiwan; aleksandr.a.spivakov@gmail.com (A.A.S.); bek106006@nptu.edu.tw (Y.-C.C.); yingzhen0307@gmail.com (Y.-Z.C.)
* Correspondence: crlinspin@gmail.com

Abstract: Pyrrhotite nanoparticles with 5C and 3C superstructures were synthesized via a simple one-step thermal decomposition method in which hexadecylamine was used as a solvent at various reaction temperatures (T_R). Structural analysis showed that at T_R = 360 °C, almost uniform in size and shape Fe_7S_8 nanoparticles with 3C superstructure are formed, and an increase in the reaction temperature leads to the formation of Fe_9S_{10} nanoparticles (5C superstructure), herewith a significant increase in the size of nanoparticles is observed. High-temperature magnetic measurements in 5 repeated heating-cooling cycles revealed that after the first heating branch in the Fe_9S_{10} samples, the λ—Peak transition disappears, and the magnetization has a Weiss-type behavior characteristic of the Fe_7S_8 sample. The change in the behavior of magnetization can be explained by the redistribution of iron vacancies, which changes the initial phase composition of nanoparticles.

Keywords: $Fe_{1-x}S$ nanoparticles; thermal decomposition; vacancy distribution; magnetic properties; synthesis conditions

Citation: Spivakov, A.A.; Lin, C.-R.; Chang, Y.-C.; Chen, Y.-Z. Synthesis of $Fe_{1-x}S$ Nanoparticles with Various Superstructures by a Simple Thermal Decomposition Route and Their Magnetic Properties. *Nanomaterials* **2021**, *11*, 1447. https://doi.org/10.3390/nano11061447

Academic Editor: Christophe Petit

Received: 1 May 2021
Accepted: 27 May 2021
Published: 30 May 2021

1. Introduction

Natural iron sulfide minerals play an important role in geochemistry, environmental, microbiology, and marine systems [1–4], while synthesized iron sulfides have found applications in various fields [5–9]. There are a variety of iron sulfides, the main ones being pyrite (FeS_2), pyrrhotite ($Fe_{1-x}S$), mackinawite (FeS), and greigite (Fe_3S_4) [10]. Pyrrhotites have attracted great interest for a long time from both scientific [11–13] and practical points of view since they have potential practical applications in such areas as biomedicine, phase-change magnetic memory devices, water treatment, as an anode material of Li-ion batteries, and so on [14–19]. The pyrrhotite group with the general chemical formula $Fe_{1-x}S$ ($0 \leq x \leq 0.125$) includes several nonstoichiometric compounds, which are due to different concentrations of vacancies in iron atom sites [13]. Pyrrhotites have the hexagonal close-packed NiAs type structure with sulfur atoms in the hexagonal close packing, and iron atoms are located at the centers of the octahedra of the sulfur atoms; herewith, pyrrhotites demonstrate various superstructures due to the different ordering of Fe atoms and cationic vacancies [20,21]. Additionally, magnetic studies of the pyrrhotite group have shown that magnetic behavior is closely related to their composition and, at room temperature, can be divided into three regions [20,22–28]: (1) $0 \leq x \leq 0.05$—Stoichiometric or almost stoichiometric antiferromagnetic troilite (space group $P\bar{6}2c$) with 2C superstructure (lattice parameters $a = \sqrt{3}A$, $c = 2C$, where A and C—The axes of the NiAs subcell); (2) $0.11 < x \leq 0.125$—Monoclinic or hexagonal ferrimagnetic pyrrhotite with 4C superstructure (1A, $2\sqrt{3}A$, 4C), which can be considered as a derivative of the NiAs structure of FeS by the removal of one-eighth iron atoms. As a result, a structure is formed in which close-packed layers of sulfur atoms alternate with layers fully occupied with Fe atoms and layers of Fe positions with vacancies. The ferrimagnetic behavior is associated with an uncompensated moment arising from the presence of vacancies in alternating layers; (3) $0.05 < x \leq$

0.11—Hexagonal pyrrhotites in which "λ—Peak transition" between an antiferromagnetic and ferrimagnetic states takes place. In this range, a set of so-called "NC" pyrrhotite superstructures (a = 2A; c = NC, $5 \leq N \leq 11$) is formed, and some pyrrhotites in the range may represent ordered phases with defined compositions, such as Fe_9S_{10} (5C), $Fe_{10}S_{11}$ (11C), and $Fe_{11}S_{12}$ (6C), however, partial ordering in these systems may also occur. Such superstructures are described in terms of stacking of fully occupied and ordered defective iron layers normal to the c-axis, and each such structure is related with a regular succession of such layers, corresponding to an integral supercell multiplicity N (or non-integral N in the case of deviations from the ordered succession, which leads to an incommensurate c-axis).

One of the reasons limiting the development and study of iron sulfides for practical application is their relatively complex synthesis, therefore, various methods for the synthesis of iron sulfides have been described in the literature, such as electrospinning [29], the toluene-thermal process [30], freeze-drying process [31], hot injection chemical synthesis [8], and so on. Iron sulfides can usually be obtained from their respective minerals via mining and separation. Among the synthesis methods, one of the most common is the high-temperature heat treatment process of exactly weighed quantities of elements Fe and S [21,24,32–34]. However, this method proceeds under complicated conditions such as low vacuum and high temperature and is also time-consuming. Moreover, this method allows, as a rule, to obtain bulk samples, while nanosized particles are of particular interest for some applications. Hydrothermal (solvothermal—developed based on the hydrothermal synthesis, but with using organic solvents) methods have been used for the fabrication of various iron sulfide nanoparticles [14,35–37]. However, these methods have a long reaction time and proceed in a sealed environment at high pressures and temperatures [38,39]. In previous works [40,41], the thermal decomposition method has been successfully used to synthesize $Fe_{1-x}S$ nanoparticles, however, the described process was carried out in several stages with the preliminary preparation of iron-oleylamine and sulfur-oleylamine complexes, which complicates the preparation of pyrrhotite nanoparticles.

In this study, pyrrhotite nanoparticles, namely Fe_7S_8 and Fe_9S_{10}, were synthesized via a simple one-step thermal decomposition method in which hexadecylamine was used as a solvent. Moreover, the process proceeds at atmospheric pressure and does not require sophisticated equipment, making it easily reproducible. The effect of the reaction temperature on the phase formation and morphology of the obtained nanoparticles was investigated, and their magnetic properties were discussed.

2. Synthesis and Experimental Techniques

In the present research, $Fe_{1-x}S$ samples were synthesized by the thermal pyrolysis method using iron (III) nitrate nonahydrate ($Fe(NO_3)_3 \cdot 9H_2O$) (Merck Millipore), sulfur powder (PanReac AppliChem ITW Reagents), and hexadecylamine (Fisher Scientific International, Inc.) (HDA). All the reagents were of analytical grade and were used without any further purification. In a typical synthesis process, 1-hexadecylamine was melted at 80 °C in a three round-bottomed flask, and then $Fe(NO_3)_3 \cdot 9H_2O$ and sulfur powder were added. The mixture was heated to 120 °C and kept at this temperature for 30 min under magnetic stirring to remove water. At the final stage of the process, the temperature was raised to the reaction temperatures (T_R), which varied from $360 \leq T_R \leq 400$ °C and kept at the appropriate temperatures for 1 h. To remove HDA, obtained nanoparticles were washed several times with toluene heated to 70 °C.

The phase formation of the nanoparticles obtained has been investigated using a SHIMADZU XRD-600 X-ray diffractometer (Shimadzu Corporation, Japan, Kyoto) (Cu Kα radiation, 40 kV, 30 mA, λ = 1.5418 Å) in the 2θ range 20–80°. The morphology and particle size of the nanoparticles have been characterized using the JEOL JEM-1230 transmission electron microscope (JEOL Ltd., Japan, Tokyo) operated at an accelerating voltage of 120 kV. Magnetic properties have been studied via a vibrating sample magnetometer (Lakeshore

7400 series VSM (Lake Shore Cryotronics Inc., Westerville, OH, USA) in the applied field of H = ± 15 kOe.

3. Results and Discussion

3.1. XRD Analysis

The X-ray diffraction (XRD) patterns of the as-synthesized nanoparticles are shown in Figure 1a. The peaks observed in the XRD patterns of the samples, synthesized at 380 and 400 °C, match well with hexagonal pyrrhotite $Fe_{1-x}S$ structure (JCPDS Card N° 17-0201) and do not contain traces of other phases. At the same time, for the sample synthesized at 360 °C, additional weak peaks occur at ~25.5°, 36.3 °, and 52.4 °. These peaks are consistent with JCPDS Card No. 89-1988 of cubic greigite, indicating that the sample contains a small fraction of Fe_3S_4.

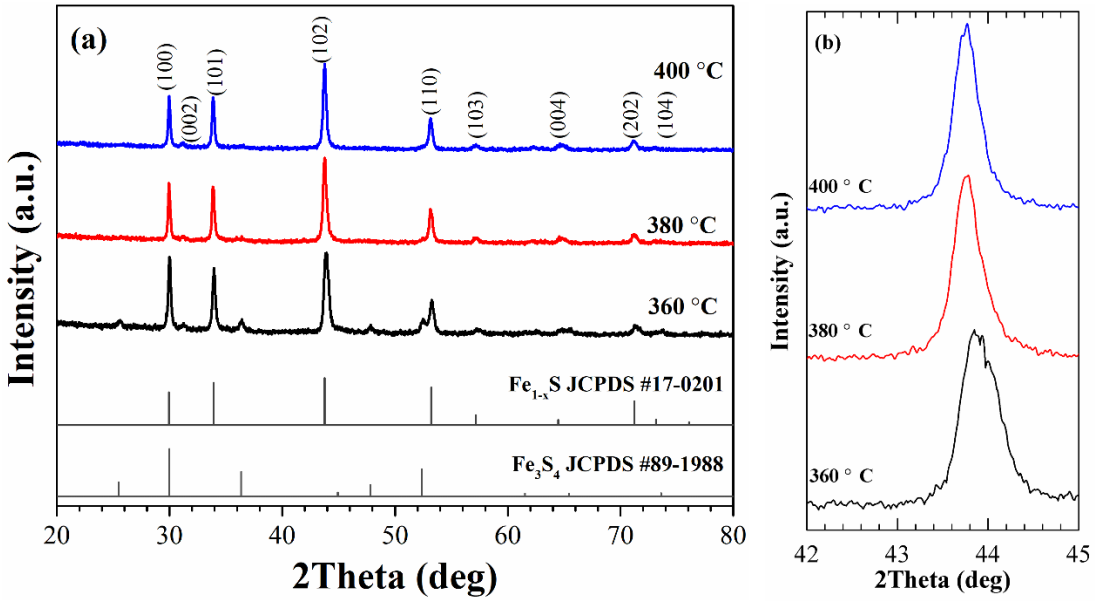

Figure 1. XRD patterns of the as-synthesized samples (**a**) and (102) diffraction peak of the samples in enlarged scale (**b**).

The identification of phase composition of the synthesized nanoparticles was carried out based on the results obtained in previous studies. Arnold [33,42] has determined a correlation between the Fe/S ratio and the position of (102) peak, which was successfully used [34] to determine the phase composition of $Fe_{1-x}S$ powders. In our experiments, the positions of the peak (102) for the samples synthesized at T_R = 360, 380, and 400 °C are at 43.91, 43.77, and 43.76°, respectively, and they can be attributed to the following compositions: Fe_7S_8 (the sample synthesized at 360 °C) and Fe_9S_{10} (the samples synthesized at 380 and 400 °C). It should be noted that the XRD pattern of the sample synthesized at 360 °C does not show the splitting of the peak (102), which is an indication of the formation of monoclinic pyrrhotite [26]. Therefore, it can be concluded that the synthesized sample is hexagonal Fe_7S_8 and has a 3C superstructure (a = 2A; c = 3C) [20,43]. Thus, the synthesis method allows controlling the phase formation of $Fe_{1-x}S$ nanoparticles by changing the reaction temperature.

3.2. TEM Data

The TEM images of the nanoparticles synthesized at 360, 380, and 400 °C are shown in Figure 2. It can be seen that nanoparticles synthesized at 360 °C are almost uniform in size and have a quasi-spherical or hexagonal shape. The particle size of the sample (inset on Figure 1a) oscillates between 25 and 50 nm and the average value obtained by Gaussian fitting is 39 nm. Meanwhile, with an increase in the reaction temperature to 380 and 400 °C, a significant increase in the upper limit of the particle size is observed (to ~350 and

550 nm, respectively). Herewith, the nanoparticles obtained at 380 °C retain accurate shape (hexagonal or triangular) with an average size of 223 nm; however, a further increase in the reaction temperature leads to the formation of mainly disordered in shape nanoparticles with an average size of 274 nm. The sharp increase in the size of $Fe_{1-x}S$ nanoparticles is related to an unconstrained dissolution-precipitation (Oswald ripening) process, in which the synthesis temperature significantly affects the growth rate of nanoparticles [44]. With an increase in the reaction temperature, the dissolution rate of small nanoparticles in a supersaturated solution increases, leading to the formation of larger nanoparticles. At the same time, their plate-like shape can be associated [14] with the preferential growth of the low-interfacial energy surface planes.

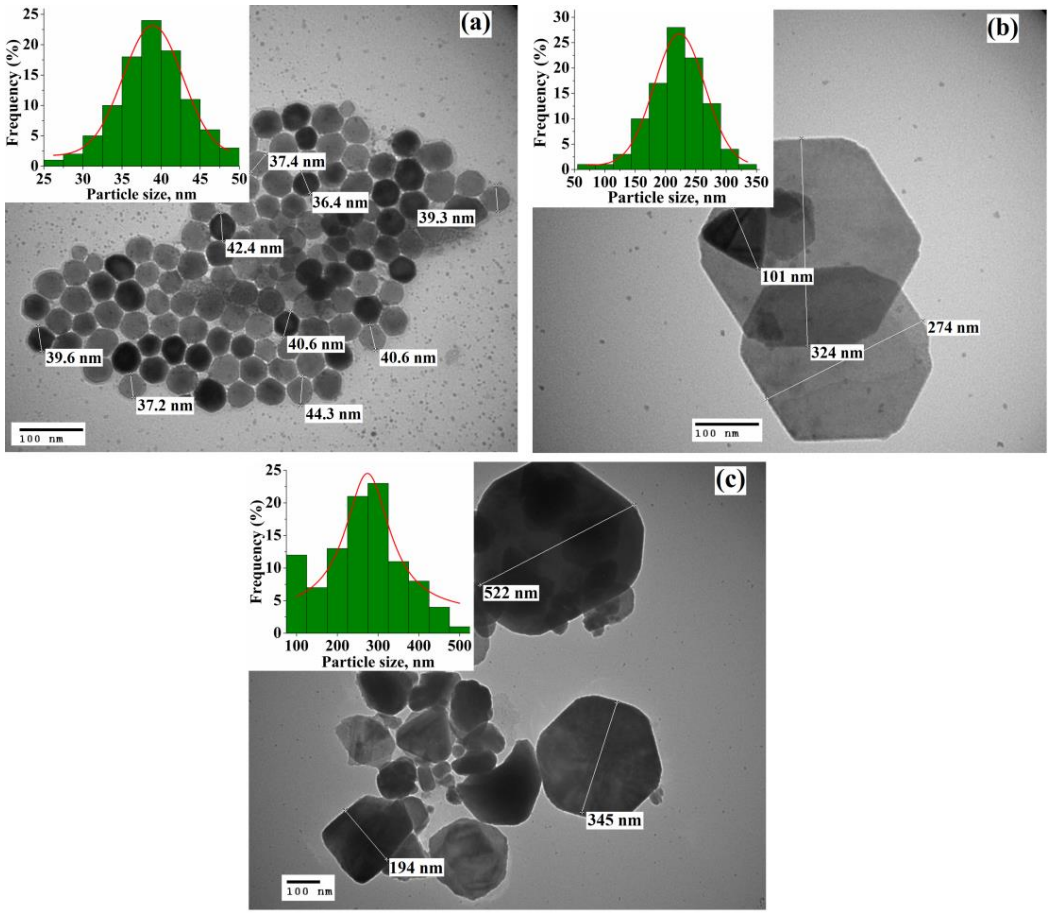

Figure 2. TEM images of the $Fe_{1-x}S$ nanoparticles synthesized at (**a**) T_R = 360 °C, (**b**) T_R = 380 °C, and (**c**) T_R = 400 °C. The insets show the particle size distribution for each sample.

3.3. Magnetic Measurements

The magnetic hysteresis loops of the synthesized nanoparticles measured at room temperature are shown in Figure 3.

As can be seen, all samples demonstrate ferromagnetic (ferrimagnetic) behavior at room temperature with hysteresis at low fields and with the values of saturation magnetization, coercivity, and remanent magnetization listed in Table 1. The larger saturation magnetization of the Fe_7S_8 sample is related to the presence of a larger number of iron vacancies in alternating layers, which leads to an increase in the uncompensated moment and an increase in M_S. Another reason for the increase in saturation magnetization is the presence of a small fraction of Fe_3S_4 identified by XRD measurements and which has a higher value of M_S. [7,45].

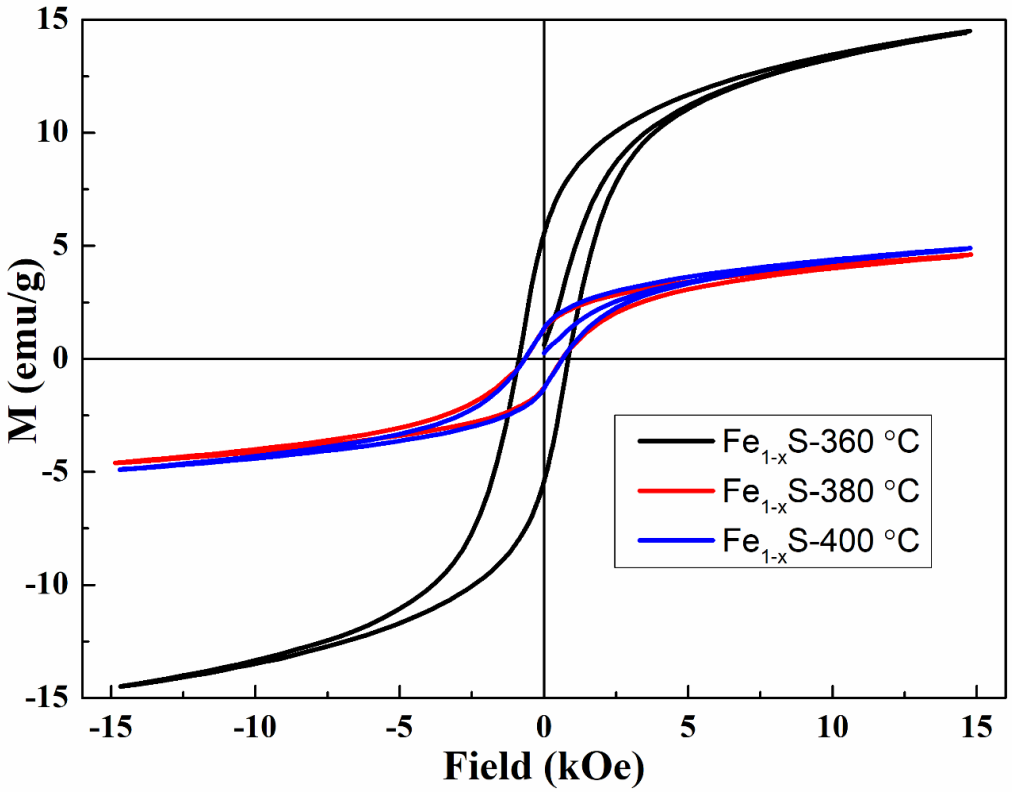

Figure 3. Magnetization curves of the samples synthesized at T_R = 360, 380, and 400 °C.

Table 1. The values of saturation magnetization (M_S), coercivity (H_C), and remanent magnetization (M_R) of the synthesized $Fe_{1-x}S$ nanoparticles.

T_R, °C	M_S, emu/g	H_C, Oe	M_R, emu/g
360	14.7	868	5.5
380	4.6	648	1.3
400	4.9	659	1.35

Temperature-dependent magnetizations of five repeated heating-cooling cycles obtained at a field of 15 kOe of the synthesized samples are presented in Figure 4 (for better visualization, only cycles 1, 3, and 5 are shown in the figure). In the first heating cycle, the Fe_7S_8 sample demonstrates mixed behavior, including λ-peak transition (starting around 425 K and with the maximum at ~475 K) and a Weiss-type component. Besides, near the Curie temperature (in the range of ~565–630 K), there is a slight deviation from the Weiss behavior associated with the presence of a small fraction of greigite in the sample.

However, already in the first cooling branch, the λ-transition is not observed, and the magnetization increases with the Weiss behavior up to room temperature. At the same time, the first heating branches of the samples obtained at T_R = 380 and 400 °C demonstrate a behavior different from that of the T_R = 360 °C sample. Magnetization started around 4.5 emu/g, consistent with the behavior of magnetic hysteresis loops of these samples. The λ—peak transition is more pronounced and starts at about 405 K with a maximum at 492 K (520 K for the sample with T_R = 400 °C), however, during the first cooling branch from 650 K, the peak transition was not reproduced, and magnetization increased with the Weiss behavior to room temperature, herewith the value of magnetization measured in the cooling regime increased significantly. Such changes in the behavior of the magnetization for the samples synthesized at T_R = 380 and 400 °C can be associated with the fact that during the first heating branch, a redistribution of vacancies between fully occupied and ordered

defective iron layers take place, which leads to a change in the initial phase composition of these samples and a change in their superstructure.

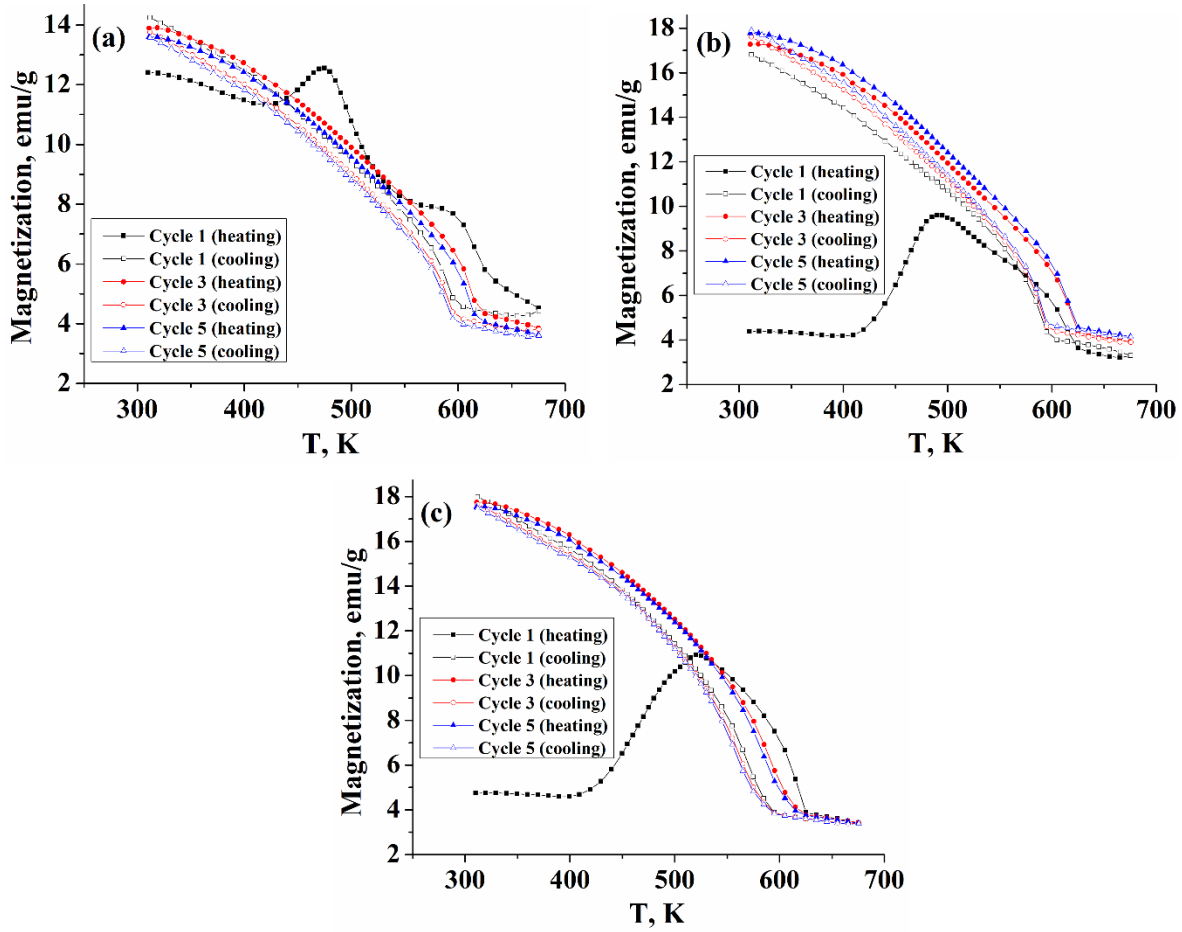

Figure 4. Temperature-dependent magnetization of the nanoparticles obtained at (**a**) T_R = 360 °C (4C), (**b**) T_R = 380 °C (5C), and (**c**) T_R = 400 °C (5C).

The results of repeated heating/cooling cycles show that in other cycles for all samples, the λ-anomaly is not observed, and the magnetization demonstrates only Weiss-type behavior, herewith the Curie transition on the cooling curves is behind the heating curves by about 30 K. The authors of work [26] have found that for peak-type pyrrhotite with composition $Fe_{0.906}S$, the λ-anomaly is recovered upon cooling the sample, herewith, the process is accompanied by the formation of a Weiss-type component, and such behavior is reproduced in the next heating-cooling cycle. The authors concluded that during heating, the peak-type pyrrhotite (with an antiferromagnetic structure) was partially converted into Weiss-type pyrrhotite (with a ferrimagnetic structure) and that this structure is partially retained upon cooling. However, for the Fe_9S_{10} samples synthesized in this work (the ordered phase Fe_9S_{10} corresponds to the composition $Fe_{0.9}S$ [21]), the λ-anomaly is not observed both in the first cooling branch and in subsequent heating-cooling cycles, that demonstrate only the Weiss-type behavior, characteristic of ferrimagnetic pyrrhotites, which is consistent with the assumption that an irreversible change in the superstructure of the samples occurs during the first heating branch.

The samples after five heating-cooling cycles were again subjected to XRD analysis to compare the phase compositions before and after high-temperature magnetic measurements. The obtained XRD data after heating/cooling cycles demonstrate that the synthesized samples are stable and do not degrade during the measurements.

As can be seen from Figure 5a, in the sample synthesized at 360 °C, except for the original peaks, an unidentified peak appears at 33.1°, while the peak (102) position did not change (Figure 5b). At the same time, for the samples obtained at T_R = 380 and 400 °C, a shift of the peak (102) towards larger angles (~44° for both samples) is observed. Thus, it can be concluded that the phase composition of these two samples changed from Fe_9S_{10} to Fe_7S_8 and high-temperature magnetic measurements led to a change in the superstructure of the samples with 5C to 3C.

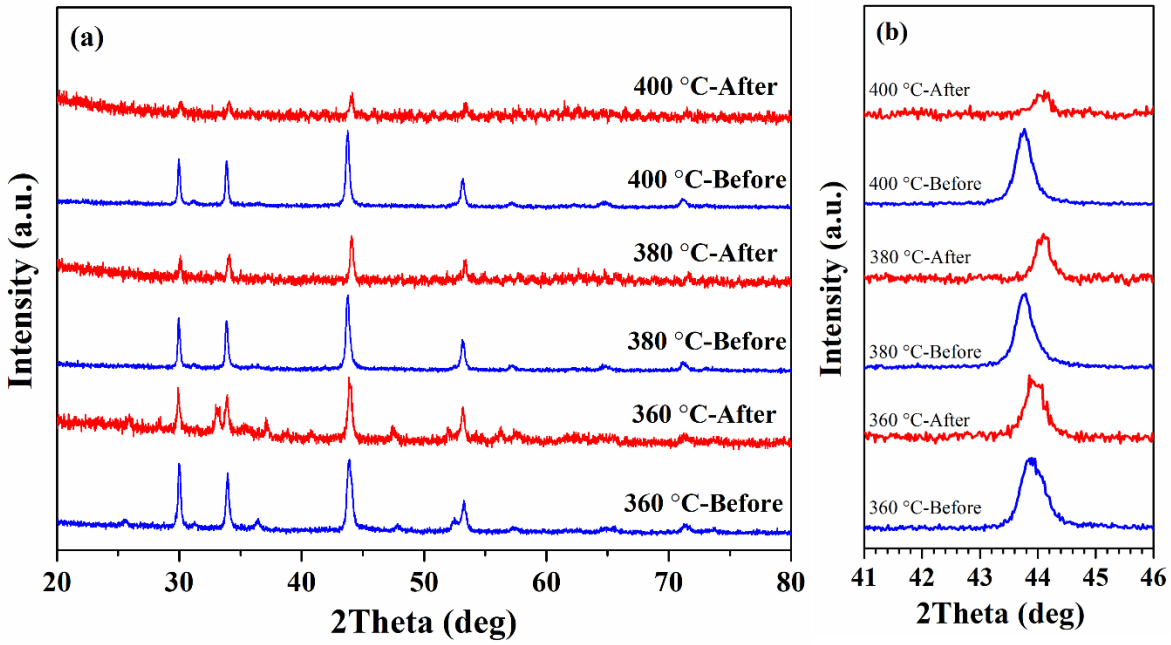

Figure 5. (**a**) XRD patterns of as-synthesized and after five heating-cooling cycles $Fe_{1-x}S$ nanoparticles; (**b**) (102) diffraction peak of the samples before and after high-temperature magnetic measurements in enlarged scale.

4. Conclusions

A simple thermal decomposition method involving iron (III) nitrate nonahydrate, sulfur powder, and hexadecylamine as a solvent for the synthesis of $Fe_{1-x}S$ nanoparticles is presented. The formation of Fe_7S_8 (3C superstructure) at T_R = 360 °C and Fe_9S_{10} (5C superstructure) at T_R = 380 and 400 °C nanoparticles was confirmed by structural analysis, herewith, it was found that an increase in the reaction temperature leads to a sharp increase in particle size. High-temperature magnetic measurements in five repeated heating-cooling cycles demonstrated that in the first heating branch, the samples obtained at T_R = 380 and 400 °C displayed markedly different behavior compared to the sample with T_R = 360 °C with a clearly pronounced the λ—Peak transition. However, already during the first cooling branch from 650 K, the peak transition was not reproduced, and magnetization increased with Weiss's behavior back to room temperature. The observed change in magnetization behavior is explained by a redistribution of vacancies which leads to a change in the initial phase composition, which is in agreement with the results of the structural analysis of the samples after high-temperature magnetic measurements.

Author Contributions: Conceptualization, C.-R.L.; Data curation, A.A.S.; Formal analysis, A.A.S. and C.-R.L.; Funding acquisition, C.-R.L.; Investigation, A.A.S., Y.-C.C. and Y.-Z.C.; Methodology, A.A.S., C.-R.L. and Y.-Z.C.; Project administration, C.-R.L.; Software, Y.-C.C.; Supervision, C.-R.L.; Visualization, Y.-C.C. and Y.-Z.C.; Writing—Original draft, Y.-C.C. and Y.-Z.C.; Writing—Review & editing, A.A.S. All authors have read and agreed to the published version of the manuscript.

Funding: This work was financially supported by Ministry of Science and Technology of Taiwan (Grant N° 109-2811-M-153-500- and Grant N° 109-2112-M-153-003-).

Data Availability Statement: The data presented in this study are available on request from the corresponding author. The data are not publicly available due to they also form part of ongoing research.

Acknowledgments: We thank the Precision Instrument Center of NPUST, where Transmission Electron Microscopy studies were carried out.

Conflicts of Interest: The authors declare no conflict of interest.

References

1. Vairavamurthy, M.A.; Schoonen, M.A.A.; Eglinton, T.I.; Luther, G.W.; Manowitz, B. *Geochemical Transformations of Sedimentary Sulfur*; ACS Symposium Series No. 612; American Chemical Society: Washington, DC, USA, 1995; p. 480. [CrossRef]
2. Walker, J.C.G. Global geochemical cycles of carbon, sulfur and oxygen. *Mar. Geol.* **1986**, *70*, 159–174. [CrossRef]
3. Fei, Y.; Prewitt, C.T.; Mao, H.-K.; Bertka, C.M. Structure and density of FeS at high pressure and high temperature and the internal structure of Mars. *Science* **1995**, *268*, 1892–1894. [CrossRef] [PubMed]
4. Bazylinski, D.A.; Moskowitz, B.M. Microbial biomineralization of magnetic iron minerals: Microbiology, magnetism and environmental significance. *Geomicrobiology* **1997**, *35*, 181–223. [CrossRef]
5. Xu, Q.-T.; Li, J.-C.; Xue, H.-G.; Guo, S.-P. Binary iron sulfides as anode materials for rechargeable batteries: Crystal structures, syntheses, and electrochemical performance. *J. Power Sources* **2018**, *379*, 41–52. [CrossRef]
6. Xie, J.; Zhu, Y.; Zhuang, N.; Lei, H.; Zhu, W.; Fu, Y.; Javed, M.S.; Li, J.; Mai, W. Rational design of metal organic frameworks-derived FeS_2 hollow nanocages@reduced graphene oxide for K.-ion storage. *Nanoscale* **2018**, *10*, 17092–17098. [CrossRef] [PubMed]
7. Yang, S.; Li, Q.; Chen, L.; Chen, Z.; Hu, B.; Wang, H.; Wang, X. Synergistic removal and reduction of U(VI) and Cr(VI) by Fe_3S_4 micro-crystal. *Chem. Eng. J.* **2020**, *385*, 123909. [CrossRef]
8. Yang, K.; Yang, G.; Chen, L.; Cheng, L.; Wang, L.; Ge, C.; Liu, Z. FeS nanoplates as a multifunctional nano-theranostic for magnetic resonance imaging guided photothermal therapy. *Biomatererials* **2015**, *38*, 1–9. [CrossRef]
9. Ting, Y.; His, H.-C. Iron sulfide minerals as potential active capping materials for mercury-contaminated sediment remediation: A minireview. *Sustainabaility* **2019**, *11*, 1747. [CrossRef]
10. Rickard, D.; Luther, G.W., III. Chemistry of iron sulfides. *Chem. Rev.* **2007**, *107*, 514–562. [CrossRef]
11. Mikami, I.; Hirone, T.; Watanabe, H.; Maeda, S.; Adachi, K.; Yamada, M. On the magnetic anisotropy of a pyrrhotite crystal. *J. Phys. Soc. Jpn.* **1959**, *14*, 1568–1572. [CrossRef]
12. Toulmin, P., III.; Barton, P.B., Jr. A thermodynamic study of pyrite and pyrrhotite. *Geochim. Cosmoch. Act.* **1964**, *28*, 641–671. [CrossRef]
13. Carpenter, R.H.; Desborough, G.A. Range in solid solution and structure of naturally occurring troilite and pyrrhotite. *Am. Mineral.* **1964**, *49*, 1350–1365. Available online: http://www.minsocam.org/ammin/AM49/AM49_1350.pdf (accessed on 29 May 2021).
14. Argueta-Figueroa, L.; Torres-Gómez, N.; Garcia-Contreras, R.; Vilchis-Nestor, A.R.; Martinez-Alvarez, O.; Acosta-Torres, L.S.; Arenas-Arrocena, M.C. Hydrothermal synthesis of pyrrhotite ($Fe_{x-1}S$) nanoplates and their antibacterial, cytotoxic activity study. *Progr. Nature Sci. Mater. Int.* **2018**, *28*, 447–455. [CrossRef]
15. Takayama, T.; Takagi, H. Phase-change magnetic memory effect in cation-deficient iron sulfide $Fe_{1-x}S$. *Appl. Phys. Lett.* **2006**, *88*, 012512. [CrossRef]
16. Li, J.; Zhang, X.; Wang, T.; Zhao, Y.; Song, T.; Zhang, L.; Cheng, X. Construction of layered hollow $Fe_3O_4/Fe_{1-x}S$ @MoS_2 composite with enhanced photo-Fenton and adsorption performance. *J. Environ. Chem. Eng.* **2020**, *8*, 103762. [CrossRef]
17. Pant, B.; Pant, H.R.; Park, M. $Fe_{1-x}S$ modified TiO_2 NPs embedded carbon nanofiber composite via electrospinning: A potential electrode material for supercapacitors. *Molecules* **2020**, *25*, 1075. [CrossRef]
18. Zhaoa, Y.; Wang, J.; Ma, C.; Cao, L.; Shao, Z. A self-adhesive graphene nanoscroll/nanosheet paper with confined $Fe_{1-x}S/Fe_3O_4$ hetero-nanoparticles for high-performance anode material of flexible Li-ion batteries. *Chem. Eng. J.* **2019**, *370*, 536–546. [CrossRef]
19. Mlowe, S.; Garje, S.S.; Moyo, T.; Revaprasadu, N. Magnetic iron sulfide nanoparticles for potential applications in gas sensing. *MRS Adv.* **2016**, *1*, 235–240. [CrossRef] [PubMed]
20. Wang, H.; Salveson, I. A review on the mineral chemistry of the non-stoichiometric iron sulphide, $Fe_{1-x}S$ ($0 \leq x \leq 0.125$): Polymorphs, phase relations and transitions, electronic and magnetic structures. *Phase Trans.* **2005**, *78*, 547–567. [CrossRef]
21. Nakazawa, H.; Morimoto, N. Phase relations and superstructures of pyrrhotite, $Fe_{1-x}S$. *Mater. Res. Bull.* **1971**, *6*, 345–357. [CrossRef]
22. Haraldsen, H. Über die eisen (II)-sulfidmischkristalle. *Z. Anor. Allgem. Chem.* **1941**, *246*, 169–194. [CrossRef]
23. Zapletal, K. Connection of some magnetic properties with the phase composition of natural pyrrhotites. *Stud. Geophys. Geod.* **1969**, *13*, 191–198. [CrossRef]
24. Horwood, J.L.; Townsend, M.G.; Webster, A.H. Magnetic susceptibility of single-crystal $Fe_{1-x}S$. *J. Sol. State Chem.* **1976**, *17*, 35–42. [CrossRef]
25. Elliot, A.D. Structure of pyrrhotite 5C (Fe_9S_{10}). *Act. Crystallogr. B* **2010**, *66*, 271–279. [CrossRef] [PubMed]
26. Li, F.; Franzen, H.F. Ordering, incommensuration, and phase transitions in pyrrhotite: Part II: A high-temperature X-ray powder diffraction and thermomagnetic study. *J. Solid State Chem.* **1996**, *126*, 108–120. [CrossRef]

27. Morimoto, N.; Gyobu, A.; Tsukuma, K.; Koto, K. Superstructure and nonstoichiometry of intermediate pyrrhotite. *Am. Mineral.* **1975**, *60*, 240–248. Available online: http://www.minsocam.org/ammin/am60/am60_240.pdf (accessed on 29 May 2021).
28. Koto, K.; Kitamura, M. The superstructure of the intermediate pyrrhotite. II. One-dimensional out-of-step vector of Fe vacancies in the incommensurate structure with compositional range from Fe_9S_{10} to $Fe_{11}S_{12}$. *Acta Cryst.* **1981**, *37*, 301–308. [CrossRef]
29. Ma, Z.; Sun, Z.; Qu, F. High-performance battery-type $Fe_{1-x}S$@CFs anode for all-solid-state batterytype asymmetric supercapacitor with high energy density and wide working temperature range. *Appl. Surf. Sci.* **2021**, *537*, 147817. [CrossRef]
30. Qian, X.F.; Zhang, X.M.; Wang, C.; Xie, Y.; Wang, W.Z.; Qian, Y.T. The preparation and phase transition of nanocrystalline iron sulfides via toluene-thermal process. *Mater. Sci. Eng. B* **1999**, *64*, 170–173. [CrossRef]
31. Jiang, F.; Wang, Q.; Du, R.; Yan, X.; Zhou, Y. Fe_7S_8 nanoparticles attached carbon networks as anode materials for both lithium and sodium ion batteries. *Chem. Phys. Lett.* **2018**, *706*, 273–279. [CrossRef]
32. Lux, H. *Handbook of Preparative Inorganic Chemistry*, 2nd ed.; Brauer, G., Ed.; Academic Press: New York, NY, USA, 1963; Volume 1, p. 1502.
33. Arnold, R.G. Pyrrhotite phase relations below 304 ± °C at <1 atm total pressure. *Econ. Geol.* **1969**, *64*, 405–419. [CrossRef]
34. Herbert, F.W.; Krishnamoorthy, A.; Yildiz, B.; Van Vliet, K.J. Diffusion-limited kinetics of the antiferromagnetic to ferrimagnetic λ-transition in $Fe_{1-x}S$. *Appl. Phys. Lett.* **2015**, *106*, 092402. [CrossRef]
35. Mlowe, S.; Osman, N.S.E.; Moyo, T.; Mwakikunga, B.; Revaprasadu, N. Structural and gas sensing properties of greigite (Fe_3S_4) and pyrrhotite ($Fe_{1-x}S$) nanoparticles. *Mater. Chem. Phys.* **2017**, *198*, 167–176. [CrossRef]
36. Liu, W.L.; Rui, X.H.; Tan, H.T.; Xu, C.; Yan, Q.Y.; Hng, H.H. Solvothermal synthesis of pyrite FeS_2 nanocubes and their superior high rate lithium storage properties. *RSC Adv.* **2014**, *4*, 48770–48776. [CrossRef]
37. Ding, C.; Yan, Y.; Xiang, D.; Zhang, C.; Xian, Y. Magnetic Fe_3S_4 nanoparticles with peroxidase-like activity, and their use in a photometric enzymatic glucose assay. *Microchim. Acta* **2016**, *183*, 625–631. [CrossRef]
38. Gao, M.R.; Xu, Y.F.; Jiang, J.; Yu, S.H. Nanostructured metal chalcogenides: Synthesis, modification, and applications in energy conversion and storage devices. *Chem. Soc. Rev.* **2013**, *42*, 2986–3017. [CrossRef]
39. Wu, W.; He, Q.; Jiang, C. Magnetic iron oxide nanoparticles: Synthesis and surface functionalization strategies. *Nanosc. Res. Lett.* **2008**, *3*, 397–415. [CrossRef]
40. Lin, C.-R.; Lu, S.-Z.; Lyubutin, I.S.; Korzhetskiy, Y.V.; Wang, S.-C.; Suzdalev, I.P. Synthesis and magnetic properties of iron sulfide nanosheets with a NiAs-like structure. *J. Appl. Phys.* **2010**, *107*, 09A335. [CrossRef]
41. Lyubutin, I.S.; Lin, C.-R.; Lu, S.-Z.; Siao, Y.-J.; Korzhetskiy, Y.V.; Dmitrieva, T.V.; Dubinskaya, Y.L.; Pokatilov, V.S.; Konovalova, A.O. High-temperature redistribution of cation vacancies and irreversible magnetic transitions in the $Fe_{1-x}S$ nanodisks observed by the Mossbauer spectroscopy and magnetic measurements. *J. Nanopart. Res.* **2011**, *13*, 5507–5517. [CrossRef]
42. Arnold, R.G. Range in composition and structure of 82 natural terrestrial pyrrhotites. *Can. Min.* **1967**, *9*, 31–50. Available online: https://rruff-2.geo.arizona.edu/uploads/CM9_31.pdf (accessed on 29 May 2021).
43. Fleet, M.E. The superstructures of two synthetic pyrrhotites. *Canad. J. Earth Sci.* **1968**, *5*, 1183–1185. [CrossRef]
44. Mc Cabe, W.; Smith, J.; Harriott, P. *Unit Operations of Chemical Engineering*, 5th ed.; McGraw-Hill: New York, NY, USA, 1993; p. 1130.
45. Liu, X.; Feng, C.; Bi, N.; Sun, Y.; Fan, J.; Lv, Y.; Jin, C.; Wang, Y.; Li, C. Synthesis and electromagnetic properties of Fe_3S_4 nanoparticles. *Ceram. Intern.* **2014**, *40*, 9917–9922. [CrossRef]